Experimental Mechanics manuscript No.
(will be inserted by the editor)

Debris Field Kinetics During the Dynamic Fragmentation of Polyphase Natural Ceramic Blocks

Ejecta Measurements and Damage Modes

James D. Hogan · Gregory Vincent · Robert J. Rogers · John G. Spray · Markus Schneider

Received: / Accepted:

Abstract The dynamic fragmentation of coarse and fine grained granitoid blocks during impact has been examined for energies of 1.9 kJ to 3.0 kJ and 2.7 kJ to 6.8 kJ, respectively. A particle tracking algorithm was developed to measure ejecta size and velocity at the rear of the target for a horizontal railgun arrangement. Fragments for the finer-grained material are smaller than the coarser-grained specimens as a result of enhanced comminution of fractured surfaces and increased intergranular fracture. Length scales > 6 mm contain > 80 % of the total mass and kinetic energy.

Median ejection velocities increase for increasing impact energy (range from 5 m/s to 10 m/s for both materials). These are low in comparison to incoming projectile velocity

J.D. Hogan
Department of Mechanical Engineering, University of New Brunswick, Fredericton, New Brunswick E3B 5A3, Canada
Tel.: 1-506-453-3560
Fax: 1-506-447-3004
E-mail: jd.hogan@unb.ca

G. Vincent
ISL, 5 rue du Général Cassagnou, 68300 Saint-Louis, France

R. Rogers
Department of Mechanical Engineering, University of New Brunswick, Fredericton, New Brunswick E3B 5A3, Canada

J. Spray
Planetary and Space Science Centre, University of New Brunswick, Fredericton, New Brunswick E3B 5A3, Canada

M. Scheider
ISL, 5 rue du Général Cassagnou, 68300 Saint-Louis, France

(250 m/s to 500 m/s) and indicate that the bulk of incoming energy is dissipated into forms other than kinetic energy transfer (e.g., heat and comminution). Approximately 25 % of the mass and 80 % of the kinetic energy is contained in velocities >20 m/s. The total conversion of impact energy to ejecta kinetic energy is estimated as approximately 3 % for the coarser material and 4 % for the finer grained material. The % conversion to momentum is higher, increasing from 7 % to 11 % for the coarser grained material and 21 % to 30 % for the finer grained material. This highlights the importance of momentum transfer during impact testing at low speeds into blocks.

Keywords particle tracking velocimetry · dynamic fragmentation · brittle materials · planetary materials · brittle fracture · ejecta measurements · railguns

1 Introduction

Understanding fragmentation and expulsion mechanisms [1–5] during impact into rocks is important in planetary and space science [6], blasting and mining industries [7], and in military applications [8]. Despite increased attention in associated fracture fields, such as earthquake science [9], mineral processing and numerical modelling [9], challenges still remain with integrating well characterized experimental measurements with physical failure mechanisms.

Dynamic fracture of brittle materials occurs when they are stressed beyond their Hugoniot elastic limit[1]. Tensile fracture commonly occurs in brittle materials (e.g., most planetary materials) and is related to grain orientation and size, temperature, strain-rate and pressure [12]. Fracture occurs along trajectories of maximum energy release [13] and it is typically initiated at a free surface [14]. Under quasi-static loading conditions, brittle materials fail due to the propagation of a small number of dominant flaws [15] and fracture paths are principally governed by crystal orientation [12]. Under high strain rate loading, many more flaw nucleation sites are simultaneously activated. The release of the excess strain energy from more activation sites results in the cascade of fractures over vast spatial

[1] The Hugoniot elastic limit is the limit of elastic deformation that ceramics can endure before deforming plastically or brittly under dynamic loading[10, 11].

(e.g., grain size, target thickness), velocity (e.g., shock and elastic wave speeds, ejecta velocities), and kinetic energy scales (e.g., those associated with small comminuted fragments and those with spalled ejecta). The multi-scale nature, combined with complex energy dissipation mechanisms, renders the study of the dynamic fragmentation of planetary materials challenging.

The dynamic fragmentation of brittle solids has similarities with concepts presented in the study of turbulent flows [4]. In three dimensional turbulence, the nonlinear interaction between different scales is described by the Kolmorogov-Richardson [16] direct cascade. Kinetic energy injected at large scale is transferred to smaller and smaller eddies until the remainder is dissipated through viscosity [16]. During dynamic fragmentation of brittle materials, cracks propagate and bifurcate to subsequently smaller scales (comminution) and secondary effects, such as abrasion between surfaces, promote further energy dissipation via, for example, heat, fragmentation, and plastic deformation.

Understanding dynamic fragmentation involves consideration of a set of variables, each requiring unique approaches. For example, micro-scale effects of crack propagation are currently not well understood due to the lack of availability of sensors (e.g., force) and equipment (e.g., scanning electron microscopy with ultra-high resolutions) for characterization of sub-100 μm scales. The conversion to kinetic energy of fragments and the characteristics of the ejecta field during impact testing is another aspect of dynamic fragmentation not currently well understood despite its importance in armour development [17,18,8,19,20] and impact cratering processes [21]. Solving these problems will require the combination of new analysis methods for quantifying these events during experiments and predicting them with multi-scale numerical models [22,9]. The development and applications of novel experimental techniques for impact testing is explored throughout this paper.

Impact testing with an electromagnetic railgun [23–26] is used here to study the fragmentation of solid planetary materials (i.e., rocks). The ballistic performance of ceramic-metal shielding systems [17,18,8,19,20], and the dynamic fragmentation of rocks [27–30] have previously been extensively studied using impact testing. The evaluation of these experiments have been at the bulk scale and primarily qualitative in nature [31,32,3,4]. Quan-

titative measurements, for example detailed analysis of complete fragment distributions and velocity measurements of ejected fragments [33–42], are more challenging to obtain. Ejecta size and velocity distributions are used here to better understand the dynamic fracture and fragmentation of planetary materials.

Velocity measurements of ejecta have been previously obtained by hand-tracing vector fields on photographs [40] and using post-experiment measurements of spatial distributions of mass to back-calculate necessary velocities [43]. Particle tracking velocimetry (PTV) has also been implemented to track the motion of a few ejecta over several high-speed image frames [42]. The cluttered nature of the debris field, especially for impact experiments at velocities $>$1.5 km/s [39–42, 34], and the inherent difficulty in developing associated computational algorithms renders tracking most of the individual fragments problematic. More recently, ejecta tracking methods have been developed and implemented to quantify size and velocity distributions at the rear to the target for 10 mm thick gabbro tiles at velocities between 25 m/s and 100 m/s [44]. Lower impact velocities in this study produce less cluttered debris fields, thus facilitating easier measurements.

This paper examines ejecta size and velocity measurements for impacts between 250 and 550 m/s for fine-grained and coarse-grained granitoid blocks. The blocks are 55 mm thick. Electromagnetic railgun technology is used as the launching platform. Previously developed particle tracking techniques are improved since Hogan et al. [44] to better resolve cluttered debris fields. Fracture mechanisms are characterized using scanning electron microscopy. The objective of the paper is to quantify length, mass, velocity, momentum and kinetic energy scales during impact into solid finite planetary material targets. These scales are observed to govern the ability of the body to dissipate the incoming impact energy through fracture and fragmentation and can be used to quantify important inherent features of the fragmentation process. More importantly, evaluation of scales enables a more complete and fundamental understanding of these complex events that can, in turn, be implemented in numerical models.

2 Experimental Setup and Particle Tracking Methods

The impact tests were performed at the French-German Research Institute of Saint-Louis (ISL), France using the SR 3/60 electromagnetic railgun as the launching platform. Impact energies ranged from 1.9 kJ (250 m/s) to 3.0 kJ (313 m/s) for the coarser grained granitoid blocks and 2.7 kJ (347 m/s) to 6.8 kJ (550 m/s) for the finer grained material. The coarse grained (Figure 1b) and fine (Figure 1a) granitoid blocks were approximately 120 mm by 120 mm and 55 mm in thickness. Aluminum (left in Figure 1c) projectiles (65 g) were used in the coarser grained block experiments and composite (right in Figure 1c) projectiles (45 g) were used for the finer grained granitoid block experiments. The coarser grained granitoid had noticeably more flaws and larger grains. Secondary electron (SE) and back-scattered electron (BSE) images of the fracture surfaces were obtained using a Hitachi SU-70 analytical Field Emission Scanning Electron Microscope.

A Photron APX Ultima video camera filming at a 8 kHz frame rate captured ejected fragments at the rear of the targets. Two high-powered lamps were used to back-illuminate the ejecta. Lighting has improved from previous studies to obtain better contrast between fragments and background [44]. A particle tracking algorithm written in Matlab [45] was implemented to track ejecta larger than 0.8 mm (determined by resolution of the camera) over multiple high-speed camera images.

Pre-processing involved image correction using, as examples, background removal and ejecta enhancement. Improvements have been made since Hogan et al [44] to achieve better sub-grid refinement for tracking more cluttered debris fields. This has been mainly due to improvements to the image analysis software in Matlab [45]. Ejecta velocity was obtained by first determining the location of the fragments in one frame and then matching probable locations through cross-correlation in subsequent frames based on iterative estimation of match probability. Differences in size, shape and (x,y) locations are considered. For example, fragments are assumed to move in the positive x-direction and remain ordered in space and time. Consideration of size and shape allow the larger ($>$4.5 mm) fragments to be identified. Post-processing consisted of removing erroneous vectors (mainly of smaller fragments) based on weighted averages of the well-tracked larger ejecta. Images are segmented,

and previously tracked particles are then removed. The process is then reapplied to track a new set of fragments once the field has expanded more within the view of the high speed camera.

3 Results

3.1 Qualitative analysis of the debris cloud

Initially, the qualitative nature of typical ejecta fields is examined (Figure 2). There are noticeably more smaller fragments in the finer grained material (Figure 2a) than for the larger grained (Figure 2b). With the exception of a few smaller fragments, the forward-most ejecta are larger in size for the coarser grained material. There is also a greater number of larger ejecta dispersed throughout the debris cloud in the coarser grained material (Figure 2b). Forward-most larger ejecta are smaller for the finer grained material and travel further after 10 ms, indicating they have a higher velocity.

3.2 Qualitative analysis of rear of the target

Post-impact features of typical targets are illustrated in Figure 3. Analysis of the target rear for the finer grained granitoid at 3.7 kJ (Figure 3a) reveals the formation of a Hertzian cone, initiating at the front surface and expanding through to the rear of the target. No observable cones are present in the coarser grained block at 3.0 kJ (Figure 3b), with fracturing primarily occurring along inherent larger planes of weakness (e.g., grain boundaries).

3.3 Ejecta field quantification

The ejecta fields (v_x vs v_y) for the lowest and highest energy cases for both materials are shown in Figure 4a and c. Impact energies are labelled. Corresponding plots of the resultant velocity, v, and ejecta angle (θ=arctan(v_y/v_x)) are shown in b. The resultant velocity is obtained assuming v_z=v_y. The ejecta angles are taken as the projections in the image plane and referred to the normal of the target surface. Interpretations will be made with respect to

Figure 4b and d, with Figure 4a and c used for reference. Lower velocities are bounded by $|\theta|<60^\circ$ for both materials. For the finer grained material, ejecta angles begin to decrease at approximately 6 m/s for an impact energy of 2.7 kJ J and 10 m/s for 6.8 kJ. For the coarser grained material, ejecta angles begin to decrease at approximately 6 m/s at an impact energy of 1.9 kJ and 8 m/s for 3.0 kJ. Ejecta angles are bounded by $|\theta|<$20-22° at the higher velocities for both cases. Trend curves reflecting these observations are shown in the figure.

The ratio of tracked (by the algorithm) and collected (post-impact) mass is used to scale fragment numbers and, by extension, size, mass, kinetic energy, and momentum distributions. Mass estimates for the tracked fragments are obtained by multiplying the density with the projected area (determined by the algorithm) and the minor axis (axis normal to longest axis). The mass obtained from the algorithm, mass collected following each experiment, their ratios and the non-scaled total number of fragments measured by the algorithm are displayed in Table 1.

3.4 Distribution of ejecta angles and their kinetic energy contributions

Shown in Figure 5 are the normalized distributions of ejecta angles (θ) for the lowest and highest impact energies for each material. The distribution for the FG: 2.7 kJ case is bi-modal with peaks at -10° and 20° (highlighted in Figure 5a). The low velocity crushed fragments (observed in Figure 4a) contribute to the negative peak, while the faster moving fragments correspond to the higher peak. The distribution for the CG: 1.9 kJ case is centered at approximately -15° and skewed towards negative ejecta angles. Again, these fragments are primarily from slower moving crushed fragments. The distributions for FG: 6.8 kJ and CG: 3.0 kJ are more symmetrical about 0°.

The distributions of kinetic energy among ejecta angles for the lowest and highest energy cases are shown in Figure 6. Peaks in Figure 6a (at -10° and 20°) and peaks in Figure 6c (at -8° and -15°) correspond to the bi-modal peaks in the ejecta distribution in Figure 5a and the skewed distribution in Figure 5c, respectively. Primary peaks are centered near 0° for the highest energy cases (Figure 6b and d), again corresponding to distribution centers in Figure 5b and d.

3.5 Normalized distribution of major axis dimensions and mass and kinetic energy contributions

Normalized distributions of major axis dimensions for the lowest energy cases for both materials are shown in Figure 7a and b, respectively. Major axis distributions are skewed towards the smaller fragments, with 55 % of the total number of fragments less than 3 mm for the finer grained material, and 50 % of the total number of fragments less than 3 mm for the coarser grained material.

Corresponding representative normalized distributions of mass among mass groups are shown in Figure 7c and d. Distributions for the finer grained material (Figure 7c) mostly remain at a consistent value at approximately 3 to 5 % for masses $>$100 mg and contain approximately 81 % of the total mass. Distributions of mass for the coarser grained material (Figure 7d) steadily increase in % beyond 100 mg and contain approximately 83 % of the total mass. The significant contribution to total mass among groups larger than 100 mg is important because, according to research by Kick [46], the input energy spent in fragmenting the body is proportional to the mass distribution of fragments.

Shown in Figure 8 are the distributions of kinetic energy among major axis dimensions. For all cases, larger dimensions contain significantly higher percentages of kinetic energy than smaller ones, and distributions become more flat at larger dimensions for increased impact energy. 82 % of the kinetic energy is captured in dimensions $>$ 7 mm for the FG: 2.7 kJ case and 73 % for FG: 6.8 kJ. Similar values are obtained for the coarse grain tests with 79 % of the kinetic energy contained in dimensions $>$ 7 mm for the CG: 1.9 kJ case and 74 % for CG: 3.0 kJ.

3.6 Velocity distribution and contributions of mass and kinetic energy

Shown in Figure 9 are histogram distributions of ejecta velocities. All distributions have similar shapes and are skewed towards lower velocities. This is a result of increased fragmentation ahead of the projectile. Maximum velocities increase from approximately 30 m/s for the lower energy cases to approximately 40 m/s for the higher energy cases for both

materials. These are low when considering impact velocities ranged from 250 to 550 m/s. Values of the 10^{th}, 50^{th} and 90^{th} (denoted in caption as x_{10}, x_{10}, x_{50} and x_{90}) percentiles of ejecta velocity are shown in Figure 9e. 50^{th} percentile values correspond to median values. Corresponding linear fits of the data are also shown. Slopes for the 10^{th}, 50^{th} and 90^{th} reflect the trends observed in the distributions. Namely, the expansion of ejecta velocities is more sensitive (greater slopes) for higher velocities than lower ones. Slopes for all percentiles remain statistically equivalent for both materials, highlighting the similarities of ejecta field expansion rates under these experimental conditions.

The distributions of ejecta mass among ejecta velocities groups is shown in Figure 10. Mass contained at lower velocities (e.g., $<$ 10 m/s) for the lower energy case finer grained material (Figure 10a) corresponds to finely crushed material (Figure 2a). The second concentration of mass at higher velocities (e.g., $>$20 m/s) in Figure 10a corresponds to those fewer larger fragments ejected at the foremost rear of the target (Figure 2a). The distribution of mass for the higher energy cases for the finer grained material (Figure 10b) expands about the higher velocities when the impact energy is increased. The distributions of mass among ejecta velocity groups for the coarser grained material are shown in Figure 10c and d. These distributions are more uniform (at approximately 7 %) than for the finer grained material. There is no notable change when the impact energy is increased. Velocity groups greater than 20 m/s contain 7 % of the mass for FG: 2.7 kJ and CG: 1.9 kJ and 14 % for FG: 6.8 kJ and CG: 3.0 kJ. The total contribution of mass $>$ 20 m/s is approximately 23 % for FG: 2.7 kJ and 20 % for FG: 6.8 kJ, and 29 % for CG: 1.9 kJ and 24 % for CG: 3.0 kJ.

Shown in Figure 10e are cumulative distributions of mass (normalized by total mass) for individual ejecta velocity for the lowest and highest cases for the finer grained material (black dots). Intermediate case are bounded by these curves. Also shown in the figure are curve fits (red solid and green hashed lines) in the form of:

$$C_1 x^{C_2} + C_3 exp(C_4 x) + C_5 ln(C_6 x) + C_7 exp(C_8 x) \quad (1)$$

where C_i, where i=1 to 8, is determined using a least-squares approach. Of all possible combinations (e.g., two power law or additional logarithmic functions), this functional form

provided the best fit for all impact energies. In the future, other, more simple, functional forms may be explored (e.g., known cumulative distribution functions such as logarithmic). The red solid line is for the FG: 2,710 J and the green hashed line is for the FG: 6,810 J (Figure 10e). Again, the black dots are the raw experimental data. Curve fitted exponents provide reasonable predictions of experimental results. Also shown in the figure is a curve fit for the highest energy case in the form of a single power law with an intercept (blue line). This functional form is commonly assumed when describing the distribution of mass for velocity [47]. Here it does not fit the FG: 6,810 J data well, especially for ejecta velocities > 25 m/s (Figure 10e).

Shown in Figure 10f is the cumulative distribution of mass versus velocity with curve fits in the form of equation (1) for the lowest and highest impact energy cases for the coarser grained material. The red dots are the experimental data, the blue hashed line is for CG: 1,940 J and the green hashed line is for CG: 3,040 J. Again, the functional form of equation (1) is able to predict the data well. Also, shown in Figure 10f is a power-law curve with intercept for the CG: 1,940 J (solid black line). As before, it does not predict the experimental data well.

The distributions of kinetic energy among ejecta velocity groups is shown in Figure 11. The contribution of kinetic energy for the lower energy cases is mainly contained in the higher velocities. The distributions are spread dispersed at higher impact energies, especially for velocities > 20 m/s. High ejecta velocities that contain more kinetic energy correspond to the larger fragments previously observed in Figure 2. This is especially noticeable for the coarser-grained material, where significantly larger fragments in Figure 2b trail faster-moving smaller ejecta. The total percentage of kinetic energy contained above 20 m/s, taken here as a representative velocity, is 78 % for FG: 2.7 kJ, 75 % for FG: 6.8 kJ, and 83 % for CG: 1.9 kJ, 79 % for CG: 3.0 kJ.

3.7 Normalized count of ejecta kinetic energy and contribution of total kinetic energy among kinetic energy groups

Histogram distributions of ejecta kinetic energy are shown in Figure 12. Distributions for the finer grained material (Figure 12a and b) are log-normal over six orders of magnitude. The median value increases from 10^{-4} J at lowest impact energy to 3.8×10^{-4} J at the highest impact energy. Distributions for coarser grained material (Figure 12c and d) have presumed peaks at 6.3×10^{-4} J for CG: 1.9 kJ and 7.2×10^{-3} J for CG: 3.0 kJ, with tails below 10^{-4} J ejecta kinetic energies.

Corresponding 10^{th}, 50^{th} and 90^{th} percentile values of individual ejecta are shown in Figure 12e. Power-law curve fits are also shown in the figure. Power law exponents are greater for the finer-grained material for the 10^{th} and 90^{th} percentiles. 50^{th} percentile values are similar for both materials and increase at a greater rate for the coarser grained material (power-law exponent of 2.40 vs. 1.26).

The contributions of total kinetic energy for ejecta kinetic energy groups are shown in Figure 13. Distributions are skewed towards larger ejecta kinetic energy. The total percentage contribution of kinetic energy for ejecta kinetic energies > 0.06 J is 79 % for FG: 2.7 kJ, 75 % for FG: 6.8 kJ, and 77 % for CG: 1.9 kJ, 72 % for CG: 3.0 kJ.

The total percentage of incoming impact energy converted to the kinetic energy of ejecta is shown in Figure 13e. Approximately 3 % is converted to ejecta kinetic energy for the coarser grained material and approximately 4 % is converted to ejecta kinetic energy for the finer material. Corresponding power-law curve fits are also shown. The coarser material is more sensitive (i.e., greater exponent) than the finer grained material.

3.8 Normalized count of ejecta momentum and contribution of total momentum

Histogram distributions of ejecta momentum are shown in Figure 14. These distributions are more narrow-band than the kinetic energy distributions (Figure 12). Distributions for the coarser-grained material are log-normal and, unlike their kinetic energy distributions, do not have noticeable tails. Corresponding 10^{th}, 50^{th}, and 90^{th} of ejecta momentums percentiles

for all impact momentums, with power-law curve fits, are shown in Figure 14e. Median (i.e., 50^{th} percentile values) increase at a greater rate for the coarser-grained material.

The contribution of total momentum for ejecta momentum groups is shown in Figure 15. Distributions are skewed to higher momentum groups and become flat for momentum groups $> 10^{-2}$ kg m/s. The total percentage contribution of momentum values $> 10^{-2}$ kg m/s is 63 % for FG: 2.7 kJ, 58 % for FG: 6.8 kJ, 63 % for CG: 1.9 kJ and 60 % for CG: 3.0 kJ. Lastly, shown in Figure 15e is the total percentage of incoming projectile momentum that is converted to the momentum of ejecta. The % momentum increases from 7 % to 11 % the coarser grained material and 13 % to 19 % for the finer grained material, with the coarser material being much more sensitive (i.e., greater exponent) than the finer-grained material.

3.9 Assessment of physical damage mechanisms

Examples of fracture surface features are examined in scanning electron microscope images in Figure 16. Surfaces in the high-energy case for the finer-grained material (Figure 16a) reveal complex inter-granular rupture (left) and cleavage fracture (top), as well as many smaller fragments on the surface (examples are highlighted).

Fragments were also mounted in resin and polished to investigate intra-fragment features. Significant intra-fragment fracture also occurs under these experimental conditions (Figure 16b). Fractures inside fragments are a combined result of propagating fracture due to impacts and the collisions among adjacent fragments and the release of elastic waves during fracture. These fractures enhance energy dissipation. Some flaws are also observed in Figure 16b. Associated micro-scale consequences of fracture are shown in Figures 16c and d. The interaction of surface asperities under large contact pressures can result in micro-cutting (Figure 16c) in quartz and the generation of sub-10 μm fragments in plagioclase (Figure 16d). These processes occur at very small scales, and are difficult to capture in numerical modelling and to systematically study.

4 Summary and Implications

A particle-tracking algorithm has been developed to investigate ejecta measurements obtained from railgun-launched impactors into coarse- (1.9 kJ to 3.0 kJ) and fine-grained (2.7 kJ to 6.8 kJ) granitoid blocks (55 mm thick). Distributions of ejecta size, velocity, mass, momentum and kinetic energy have been quantified and their inter-relationships investigated. Studies of this kind are needed for the development and validation of numerical models, which rely on well characterized experiments. In particular, challenges exist in numerical codes when implementing schemes to determine fragments (e.g., through consideration of damaged volumes), and to monitor fragments and their interactions throughout space and time [48]. Such models are computationally expensive, and replicating observable features in experiments remains difficult [49]. Experimental measurements under moderate conditions, where a detailed library of measurements can be attained rapidly once experimental setups (e.g., lighting) and particle tracking algorithms are developed, are needed in order to validate models so that they can be applied to more extreme impact conditions.

Qualitative analysis of high-speed video images and quantification of size distributions indicate that fragments are smaller for the finer grained material than the coarser grained material (55 % $<$ 3 mm vs. 50 %). This is likely a result of enhanced inter-granular fracture and subsequent comminution of the finer grained material. The contributions of mass and kinetic energy for each length scale were also examined. Masses $>$100 mg (equivalent size of 6 mm) contain approximately 80 % of the total mass for both materials for all impact energies. Length scales greater than approximately 6 mm contain 80 % of the total kinetic energy. These are slightly smaller than for gabbro tiles [44] and is a result of increased degradation of fractured surfaces from abrasion for thicker targets. These highlight important length scales to capture energy dissipated via fragmentation [50] and kinetic energy for numerical models, where selection of length scales in finite element modelling through consideration of element size is critical when attempting to accurately model and capture the dynamic fragmentation of brittle solids.

Characterization of ejecta angle distributions revealed bi-modal peaks at -10° and 20° for the lower energy case for the finer-grained targets. The peak for the lower energy case for

the coarser-grained material was centered at -15°. Negative distribution peaks correspond to lower velocity ejecta, or those severely crushed during impact that are more affected by gravity. Briefly, the effect of gravity is considered: at low impact speeds, the effect gravity on ejecta velocity results can yield negative y-velocities of 1.2 m/s to 1.7 m/s. At 0.5 m/s to 1 m/s x-velocities, these correspond to variations in ejecta angles of 20° to 35°. This roughly corresponds to the shift of the ejecta field at later times (Figure 4). In the future, the effect of gravity on ejecta velocities can be included in the algorithm. Other features, such as wake dynamics, also affect the measured ejecta angle. It is worth noting that ambient conditions and atmospheric effects (dynamic deceleration) also affect the trajectories of the very fine ($< 60\mu$m) ejecta [51].

The ejecta angle distributions become more symmetrical about 0° as the impact energy is increased, suggesting more symmetric fragmentation around the projectile and ejection from the target. Distribution peaks in ejecta angle measurements are associated with highs in the distribution of kinetic energy with impact angle. This highlights the importance of the inter-relation between fragmentation (through characterization of normalized counts of ejecta distributions) and kinetic energy transfer (through characterization of the kinetic energy dependence on ejecta angle distributions). In particular, larger fragments are spalled from the target rear and the available space allows for subsequent fragment ejection. An increase in fragmentation in the ejection of larger fragments (those with larger KE) is observed in the results.

Median resultant ejection velocities increase for increasing impact energy and are comparable for both materials (range from 5 m/s to 10 m/s). These are low in comparison to incoming projectile velocities (250 m/s to 500 m/s) and indicate that the bulk of incoming energy is dissipated into forms other than kinetic energy transfer (e.g., heat and comminution). As an aside, the resultant velocity for each ejecta is obtained assuming v_z=v_y. This assumption preserves the true distribution of v_z (i.e., normal distribution about 0 m/s with maxima and minima of the absolute value of the maximum v_y). The true distribution of v_z is known from ongoing ejecta measurements. The v_z=v_y assumption was chosen to attempt to better represent the total KE of the ejecta (one of the important results from this study). The

lower bound for % ejecta KE values occurs when it is assumed that v_z=0. The upper bound occurs when each v_z is equal to the maximum v_y. Values are between these two bounds when it is assumed that v_z=v_y. As a comparison, values of total % KE were computed with vz=0 (which produces the greatest difference in values). On average, these values were less by 8 % for KE (range 3% to 13% in difference). Low differences in %KE for the two assumption occur because the streamwise velocity (v_x) and those with low ejection angles (Figure 6) contain most of the %KE. More specifically, the contribution KE for v_z and v_y is low in comparison to v_x. The effect of this assumption on the distribution of KE among ejecta length and velocity (where fragments $>$ 6 mm contain $>$ 80 % of KE) is also minor (no greater than 10 % for each case). In the future, values of v_z will be assigned assuming it has normal distribution about 0 m/s and can range from plus of minus v_{maxy}.

Distributions of mass and kinetic energy among ejecta velocity groups were also considered. Approximately 25 % of the mass is contained in velocities $>$20 m/s, while 80 % of the kinetic energy is captured. This mass is mainly contained in the larger fragments ejected from the rear of the target. Cumulative distributions of mass with respect to ejecta velocity reveal reasonable prediction of the lowest and highest energy cases for both materials using an additive logarithm, power-law and exponential function (equation (1). This functional form is more complicated than commonly used power-law functions [47], which were not able to predict the data here. Combined, these results provide important velocity scales during the dynamic fragmentation of planetary materials and are critical in the development and validation of numerical models.

Distributions of ejecta kinetic energy and momentum were also examined. Rotational kinetic energy is assumed to be negligible. As an example, a 2 mm fragment rotating at 1 rad/s (estimated from video images) has a rotational kinetic energy of 1.7E-10 J. A similar fragment with a translational velocity of 0.5 m/s has a kinetic energy of 1.3E-5 J. Rotational energy is 5 orders of magnitude smaller and is, therefore, considered negligible. Log-normal distributions of ejecta kinetic energy span six orders of magnitude. Momentum distributions were found to be more narrow-band. The total percentage contribution of kinetic energy for ejecta kinetic energies $>$ 0.06 J is $>$ 70 %. Similar trends were observed for momentum

groups, where > 60 % is contained $> 10^{-2}$ kg m/s. Results highlight the equal contribution of the larger groups (approximately 7% for each group) and the importance of the larger rear fragments to momentum and kinetic energy contributions. Median ejecta kinetic energy and momentum can be used in to compare among other processes and experimental configurations (e.g., target thickness, ceramic/metal target).

The total conversion of impact energy to ejecta kinetic energy was estimated as approximately 3 % for the coarser material and approximately 4 % for the finer grained material. Values are slightly higher for higher impact energies. The % conversion to momentum is significantly higher, increasing from 7 % to 11 % for the coarser grained material and 13 % to 19 % for the finer grained material as the impact energy is increased. These are a result of low velocities and substantial fragmentation, and highlights the importance of momentum and kinetic energy transfer in impact events.

Lastly, micro-scale failure mechanisms were characterized and results indicate that transgranular (i.e., through grains) fracture is an important mechanism of fragmentation. An example includes cleavage fracture. Intergranular fracture (i.e., along grain boundaries) primarily occurs inside fragments. Micro-scale cutting and fragmentation were also observed. The incorporation of micro-scale contact and fragmentation effects, and the inclusion of multi-phases materials, into numerical code warrants further consideration as these micro-scale processes likely account for the majority of the energy dissipation during impact.

4.1 Future Considerations for Particle Tracking

Mirrors or an additional camera would provide an improved measure of the ejecta size and velocity (i.e., v_x, v_y, and v_z). Field shape formation (e.g., hemispherical growth vs jetting) may be better understood through comparison of ejecta angles (e.g., v_x-v_y angle, and v_x-v_z angle), provided that two image pairs could be synchronized in time and space so that they can be correlated. Synchronizing video imaging would require intersecting laser planes (e.g., a cone laser and a sheet laser) and the implementation of a more advanced probable-match algorithm.

Additional challenges arise when extending a three dimensional tracking algorithm to higher speeds (e.g., hypervelocity impacts). At higher impact speeds, the debris cloud is more chaotic and more dust is formed. A combined particle image velocimetry (PIV) approach, which uses an Eulerian reference frame and estimates velocities of gridded cells, can be used with image enhancement. Note that particle tracking velocimetry uses a Lagrangian approach to determine the velocity field in the present experiments. Image analysis can be used to determine ejecta centroids, which can then be projected onto the velocity field (obtained with PIV). This method would be computationally less expensive than attempting to track individual ejecta. Such measurement techniques are currently being developed and results can be contrasted with a single camera view in the future.

5 Concluding Remarks

The dynamic fragmentation during impact of coarse- and fine-grained granitoid blocks has been examined for impact energies ranging from 1.9 kJ to 3.0 kJ and 2.7 kJ to 6.8 kJ, respectively. An ejecta tracking algorithm was implemented to quantify ejecta size, velocity, mass, momentum and kinetic energy distributions. Fragments for the finer-grained material are smaller than the coarser-grained specimens as a result of enhanced comminution of fractured surfaces and increased intergranular fracture. Length scales > 6 mm contain > 80 % of the total mass and kinetic energy. Median length scales decrease for increasing impact energy. Length scale quantification is import in the selection of element sizes in numerical models, where the goal is to capture the majority of energy dissipation.

Velocity and ejecta angle distributions were also quantified. The primary ejecta angle direction was found to be dependent on the primary direction of kinetic energy of the launched ejecta (i.e., peak in KE(θ)). This is a result of more space for fragmentation when larger fragments are ejected from the rear of the target. Median ejection velocities increase for increasing impact energy (range from 5 m/s to 10 m/s for both materials). These are low in comparison to incoming projectile velocity (250 m/s to 500 m/s) and indicate that the bulk of incoming energy is dissipated into forms other than kinetic energy transfer (e.g., heat). Approximately 25 % of the mass and 80 % of the kinetic energy is contained in velocities

>20 m/s. New functional forms of the cumulative distribution of mass for ejecta velocity were also explored. Low velocities and substantial fragmentation of the blocks results in greater percentage conversion of momentum to ejecta momentum (i.e., 7 % to 11 % for the coarser grained material and 13 % to 19 % for the finer grained material). The total conversion of impact energy to ejecta kinetic energy is estimated as approximately 3 % for the coarser-grained material and approximately 4 % for the finer material. Lastly, physical features of the failure surfaces suggest micro-scale contact and fragmentation effects, and the inclusion of multi-phases materials, should be considered in numerical codes as these micro-scale processes likely account for the majority of the energy dissipation during impact.

Advances in high-speed image processing have made it possible to study the dynamic fragmentation of brittle solids in greater depth. The quantification of important ejecta scales is critical for the development and verification of theoretical and numerical models. Application of current techniques to metal and metal-ceramic shielding systems would greatly improve application of these energy dissipation systems. The data presented here provides a framework to facilitate future studies. An improved understanding of the dynamic fragmentation of brittle materials will involve a coherent approach combining fracture measurements and theoretical modelling with modern laboratory experimental tools and large-scale computer simulation.

Acknowledgements This work was supported by a Natural Sciences and Engineering Research Council (NSERC) PGS-D scholarship to JDH and funding from NSERC, the Canada Research Chairs program and the Canada Foundation for Innovation to JGS. The authors would also like to thank the effort and contribution during the experimental phase of the study of Yannick Boehrer, David Bluntzer and Philippe Baumann at ISL. Suporn Boonsue kindly assisted with the electron microscopy. Planetary and Space Science Centre contribution 75.

References

1. N. Mott, A theory of the fragmentation of shells and bombs, Technical Report AC4035, United Kingdom Ministry of Supply (May 1943).

2. D. Grady, The spall strength of condensed matter, Journal of Mechanics Physics of Solids 36 (1988) 353–384.
3. D. A. Shockey, D. R. Curran, L. Seaman, J. T. Rosenberg, C. F. Petersen, Fragmentation of rock under dynamic loads, International Journal of Rock Mechanics and Mining Sciences 11 (8) (1974) 303 – 317.
4. D. E. Grady, Length scales and size distributions in dynamic fragmentation, International Journal of Fracture 163 (1–2) (2009) 85–99.
5. M. A. Meyers, C. T. Aimone, Dynamic fracture (spalling) of metals, Progress in Materials Science 28 (1) (1983) 1 – 96.
6. B. M. French, Traces of Catastrophe: A Handbook of Shock-Metamorphic Effects in Terrestrial Meteorite Impact Structures, LPI Contribution No. 954, Lunar and Planetary Institute, Houston, 1998.
7. J. Aler, J. D. Mouza, M. Arnould, Measurement of the fragmentation efficiency of rock mass blasting and its mining applications, International Journal of Rock Mechanics and Mining Science and Geomechanics Abstracts 33 (2) (1996) 125 – 139.
8. E. Strassburger, Ballistic testing of transparent armour ceramics, Journal of the European Ceramic Society 29 (2) (2009) 267 – 273, special Issue on Transparent Ceramics.
9. B. N. Cox, H. Gao, D. Gross, D. Rittel, Modern topics and challenges in dynamic fracture, Journal of the Mechanics and Physics of Solids 53 (3) (2005) 565 – 596.
10. F. Zhou, J. F. Molinari, K. Ramesh, Analysis of the brittle fragmentation of an expanding ring, Computational Materials Science 37 (1-2) (2006) 74 – 85.
11. F. Zhou, J. F. Molinari, K. T. Ramesh, Effects of material properties on the fragmentation of brittle materials, International Journal of Fracture 139 (2006) 169–196.
12. C. Rong, Y. Xiao-Xin, X. Hung-Sen, Studies of the fracture of gabbro, International Journal of Rock Mechanics and Mining Sciences 16 (3) (1979) 187 – 193.
13. C. Kocer, R. E. Collins, Angle of hertzian cone cracks, Journal of the American Ceramic Society 81 (7) (1998) 1736 1742.
14. P. H. Shipway, I. M. Hutchings, Fracture of brittle spheres under compression and impact loading. i. elastic stress distributions, Philosophical Magazine A 67 (6) (1993) 1389–1404.
15. V. Shenoy, K.-S. Kim, Disorder effects in dynamic fragmentation of brittle materials, Journal of the Mechanics and Physics of Solids 51 (1112) (2003) 2023 – 2035.
16. A. Kolmogorov, The local structure of turbulence in incompressible viscous fluid for very large reynolds numbers, Proc. R. Soc. Lond. A 434 (1991) 9–13.
17. D. A. Shockey, A. Marchand, S. Skaggs, G. Cort, M. Burkett, R. Parker, Failure phenomenology of confined ceramic targets and impacting rods, International Journal of Impact Engineering 9 (3) (1990) 263 – 275.
18. E. S. C. Chin, Army focused research team on functionally graded armor composites, Materials Science and Engineering A 259 (2) (1999) 155 – 161.

19. D. P. Goncalves, F. C. L. de Melo, A. N. Klein, H. A. Al-Qureshi, Analysis and investigation of ballistic impact on ceramic/metal composite armour, International Journal of Machine Tools and Manufacture 44 (2-3) (2004) 307 – 316.

20. M. L. Wilkins, Mechanics of penetration and perforation, International Journal of Engineering Science 16 (11) (1978) 793 – 807, special Issue: Penetration Mechanics.

21. J. G. Spray, Frictional melting processes in planetary materials: From hypervelocity impact to earthquakes, Annual Review of Earth and Planetary Sciences 38 (1) (2010) 221–254.

22. M. Marder, S. Gross, Origin of crack tip instabilities, Journal of the Mechanics and Physics of Solids 43 (1) (1995) 1 – 48.

23. L. Holland, Distributed-current-feed and distributed-energy-store railguns, Magnetics, IEEE Transactions on 20 (2) (1984) 272 – 275.

24. A. Poltanov, A. Kondratenko, A. Glinov, V. Ryndin, Multi-turn railguns: concept analysis and experimental results, Magnetics, IEEE Transactions on 37 (1) (2001) 457 –461.

25. J. Pappas, D. Piccone, Power converters for railguns, Magnetics, IEEE Transactions on 37 (1) (2001) 379 –384.

26. M. Schneider, O. Liebfried, V. Stankevic, S. Balevicius, N. Zurauskiene, Magnetic diffusion in railguns: Measurements using cmr-based sensors, Magnetics, IEEE Transactions on 45 (1) (2009) 430 –435.

27. K. A. Holsapple, R. M. Schmidt, On the scaling of crater dimensions 1: Explosive processes, Journal of Geophysics 85 (1980) 7247–7256.

28. K. A. Holsapple, R. M. Schmidt, On the scaling of crater dimensions 2: Impact processes, Journal of Geophysics 87 (1982) 1849–1870.

29. J. Walker, S. Chocron, Near-earth object deflection using conventional explosives, International Journal of Impact Engineering 35 (12) (2008) 1473 – 1477.

30. T. Saito, K. Kaiho, A. Abe, M. Katayama, K. Takayama, Hypervelocity impact of asteroid/comet on the oceanic crust of the earth, International Journal of Impact Engineering 35 (12) (2008) 1770 – 1777.

31. J. D. Hogan, J. G. Spray, R. J. Rogers, S. Boonsue, G. Vincent, M. Schneider, Micro-scale energy dissipation mechanisms during dynamic fracture in natural polyphase ceramic blocks, International Journal of Impact Engineering.

32. D. E. Grady, M. E. Kipp, The micromechanics of impact fracture of rock, International Journal of Rock Mechanics 16 (5) (1979) 293 – 302.

33. I. Giblin, New data on the velocity-mass relation in catastrophic disruption, Planetary and Space Science 46 (8) (1998) 921 – 928.

34. W. K. Hartmann, Impact experiments: 1. ejecta velocity distributions and related results from regolith targets, Icarus 63 (1) (1985) 69 – 98.

35. H. Melosh, High-velocity solid ejecta fragments from hypervelocity impacts, International Journal of Impact Engineering 5 (1-4) (1987) 483 – 492, hypervelocity Impact Proceedings of the 1986 Symposium.

36. C. A. Polanskey, T. J. Ahrens, Impact spallation experiments: Fracture patterns and spall velocities, Icarus 87 (1) (1990) 140 – 155.

37. A. Nakamura, A. Fujiwara, Velocity distribution of fragments formed in a simulated collisional disruption, Icarus 92 (1) (1991) 132 – 146.

38. H. Kamminga, Life from spacea history of panspermia, Vistas in Astronomy 26 (1982) 67 – 86.

39. D. Gault, E. Heitowit, The partition of energy for hypervelocity impact craters formed in rock, Proc. 6th Hypervelocity Impact Symp (1963) 419–456.

40. A. Fujiwara, A. Tsukamoto, Experimental study on the velocity of fragments in collisional breakup, Icarus 44 (1) (1980) 142 – 153.

41. D. Braslau, Partitioning of energy in hypervelocity impact against loose sand targets, Journal of Geophysical Research 75 (20) (1970) 3987–3999.

42. B. Hermalyn, P. H. Schultz, Early-stage ejecta velocity distribution for vertical hypervelocity impacts into sand, Icarus 209 (2) (2010) 866 – 870.

43. T. Michikami, K. Moriguchi, S. Hasegawa, A. Fujiwara, Ejecta velocity distribution for impact cratering experiments on porous and low strength targets, Planetary and Space Science 55 (12) (2007) 70 – 88.

44. J. D. Hogan, J. G. Spray, R. J. Rogers, G. Vincent, M. Schneider, Dynamic fragmentation of natural ceramic tiles: Ejecta measurements and kinetic consequences, International Journal of Impact Engineering 58 (0) (2013) 1 – 16.

45. 2011 Matlab User Manual.

46. F. Kick, Das gesetz des proportionalen widerstandes und seine anwendung, Arthur Felix, Leipzig.

47. K. R. Housen, K. A. Holsapple, Ejecta from impact craters, Icarus 211 (1) (2011) 856 – 875.

48. M. Jutzi, P. Michel, W. Benz, D. C. Richardson, Fragment properties at the catastrophic disruption threshold: The effect of the parent bodys internal structure, Icarus 207 (1) (2010) 54 – 65.

49. N. Artemieva, K. Wnnemann, C. Meyer, W. Reimold, D. Stffler, Ries crater and suevite revisited: part ii modelling, Lunar Planet. Sci. 40 (Abs. 1526).

50. R. T. Hukki, Proposal for a solomonic settlement between the theories of von Rittinger, Kick and Bond, SME-AIME (220) (1961) 403 – 408.

51. P. H. Schultz, Atmospheric effects on ejecta emplacement, Journal of Geophysical Research: Planets 97 (E7) (1992) 11623–11662.

List of Figures

List of Tables

Table 1 Estimated mass tracked by the algorithm, mass collected following the experiment, and the ratio used to scale the experiments. FG: fine grained, CG: coarser grained.

Material	Energy (J)	Estimated tracked Mass[2] (g)	Collected Mass[3] (g)	Ratio
FG	2,710	348	966	0.36[4]
FG	3,730	684	1,053	0.65
FG	4,200	855	1,156	0.74
FG	4,800	864	1,252	0.69
FG	6,810	1,037	1,402	0.74
CG	1,940	490	754	0.65
CG	2,330	743	844	0.88
CG	2,500	787	916	0.86
CG	3,040	1,138	1,084	1.05

[2] These are estimated assuming an in-plane thickness.
[3] This is the mass of fragments collected after each test.
[4] The low ratio is attributed to the underestimation of in-plane thickness of larger fragments.

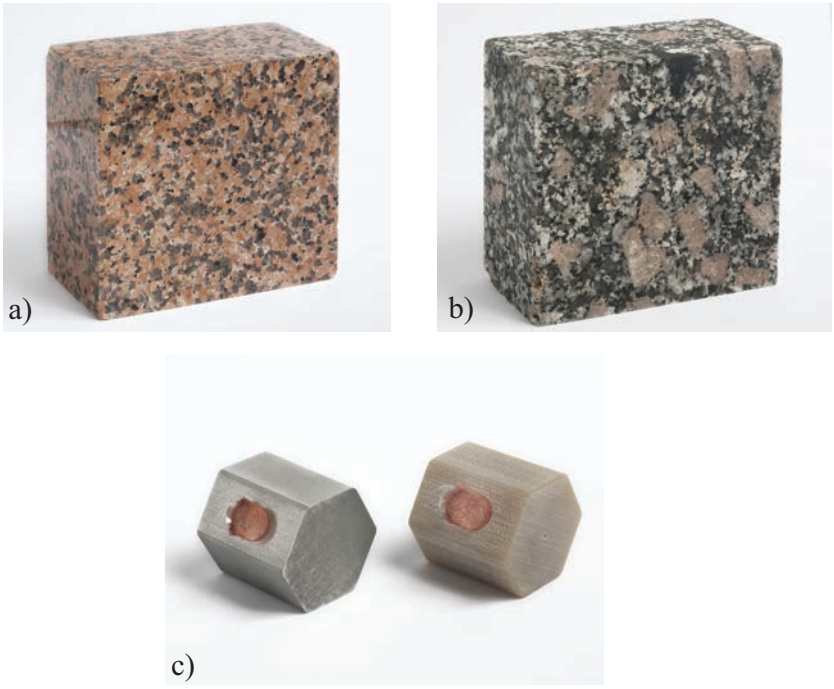

Fig. 1 Photographs of the target material: (a) finer grained granitoid and (b) coarser grained granitoid, and (c) aluminum (left) and composite (right) projectiles. The blocks are 55 mm thick and the projectiles are 32 mm in length.

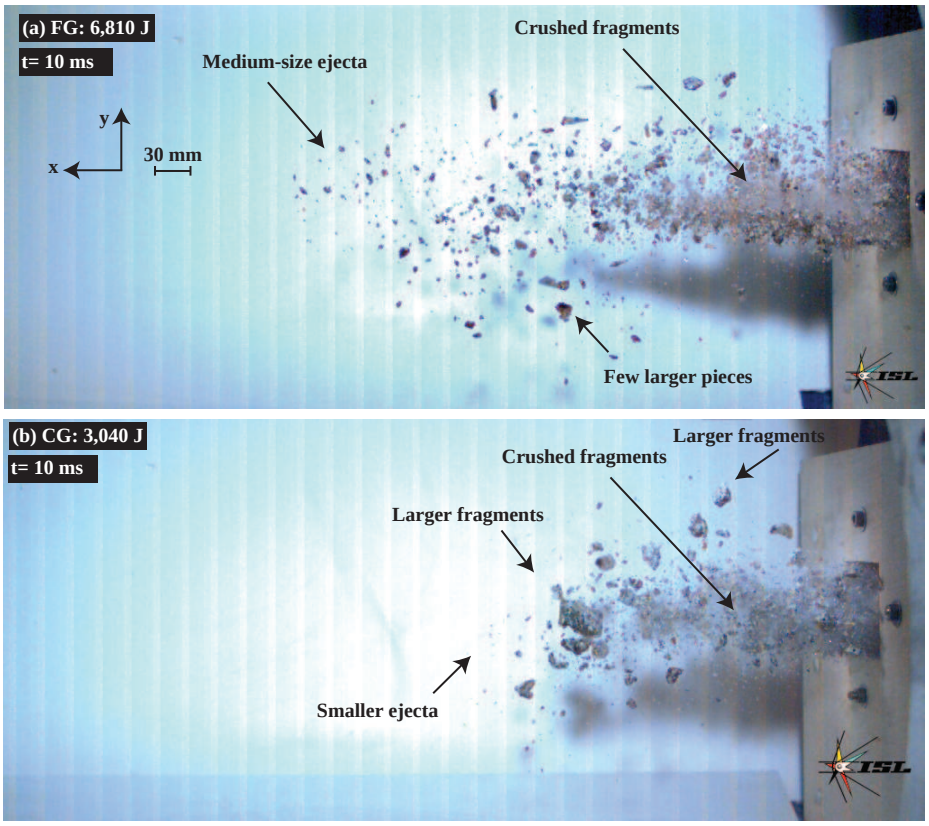

Fig. 2 Qualitative nature of the ejecta field for (a) finer grained (6.8 kJ) and (b) coarser grained material (3.0 kJ). FG: finer grained material and CG: coarser grained material. Various fragmentation types are noted.

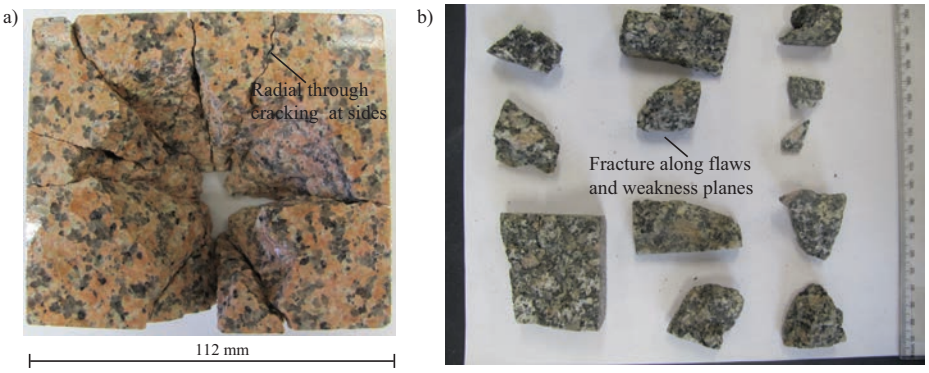

Fig. 3 Photographs of (a) target for the finer-grained material at 3.7 kJ showing Hertzian cone cracking, and (b) the residual coarser-grained target at 3.0 kJ showing fracture primarily along inherent flaws.

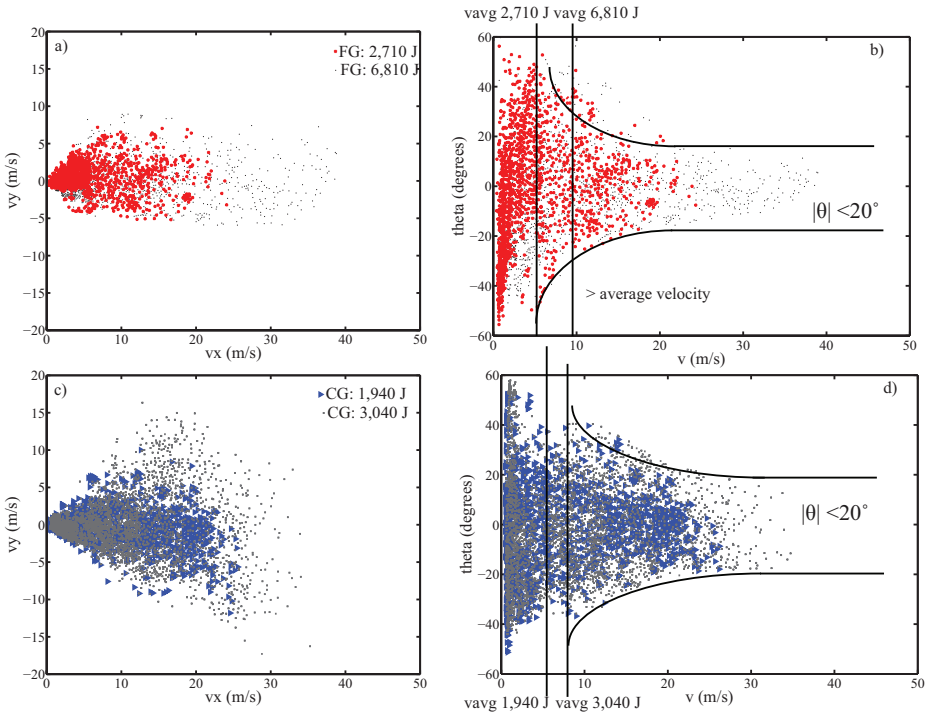

Fig. 4 The ejecta field (v_x vs v_y) for the (a) 2.7 kJ and 6.8 kJ for the finer grained material and (c) 1.9 kJ and 3.0 kJ for the coarser grained material. Corresponding plots of the resultant velocity, v, and ejecta angle (θ=arctan(v_y/v_x)) are shown in (b) and (d). Each point on the plot represents an individual ejecta and different colours indicate different tests.

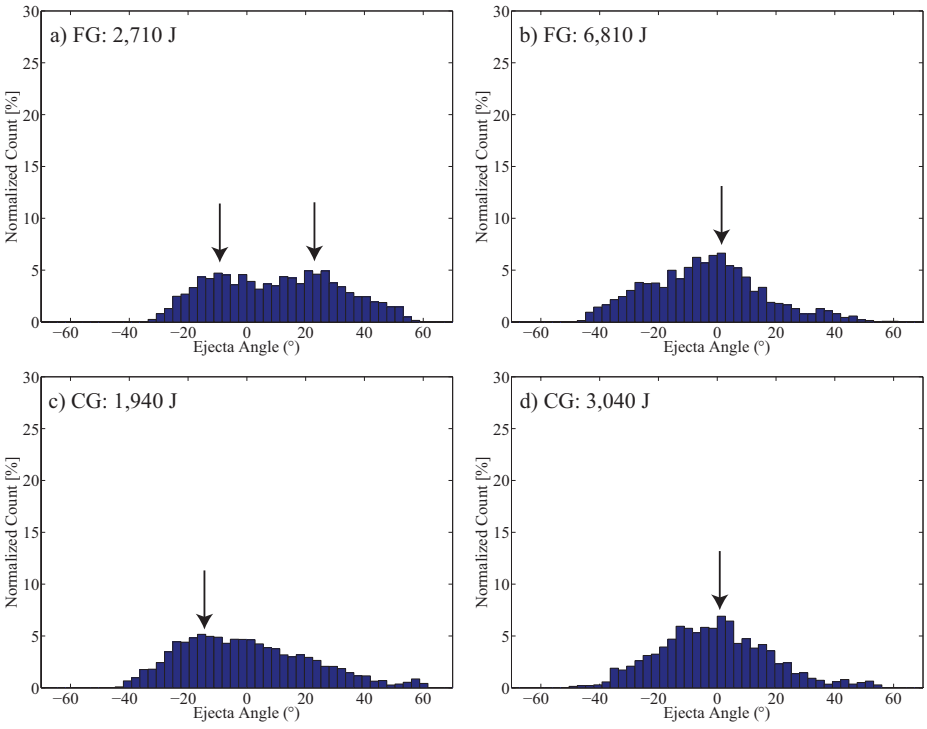

Fig. 5 Distribution of ejecta angles for: the finer grained material at (a) 2.7 kJ and (b) 6.8 KJ, and the coarser grained material at (c) 1.9 kJ and (d) 3.0 kJ. Arrows indicate presumed peaks in the distributions.

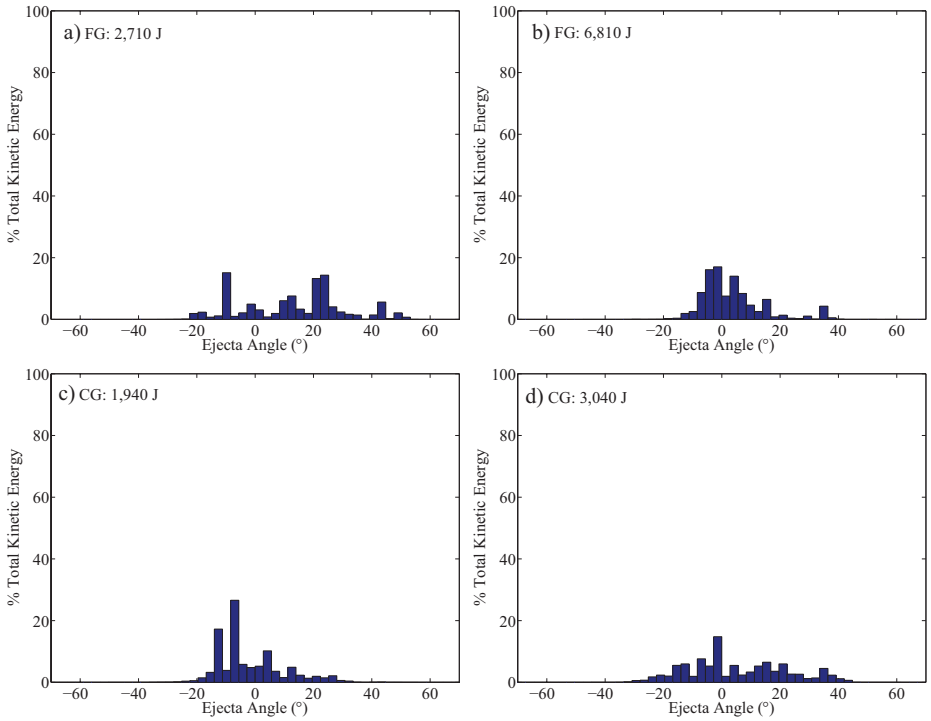

Fig. 6 Distribution of kinetic energy among ejecta angles for: the finer grained material at (a) 2.7 kJ and (b) 6.8 kJ, and the coarser grained material at (c) 1.9 kJ and (d) 3.0 kJ.

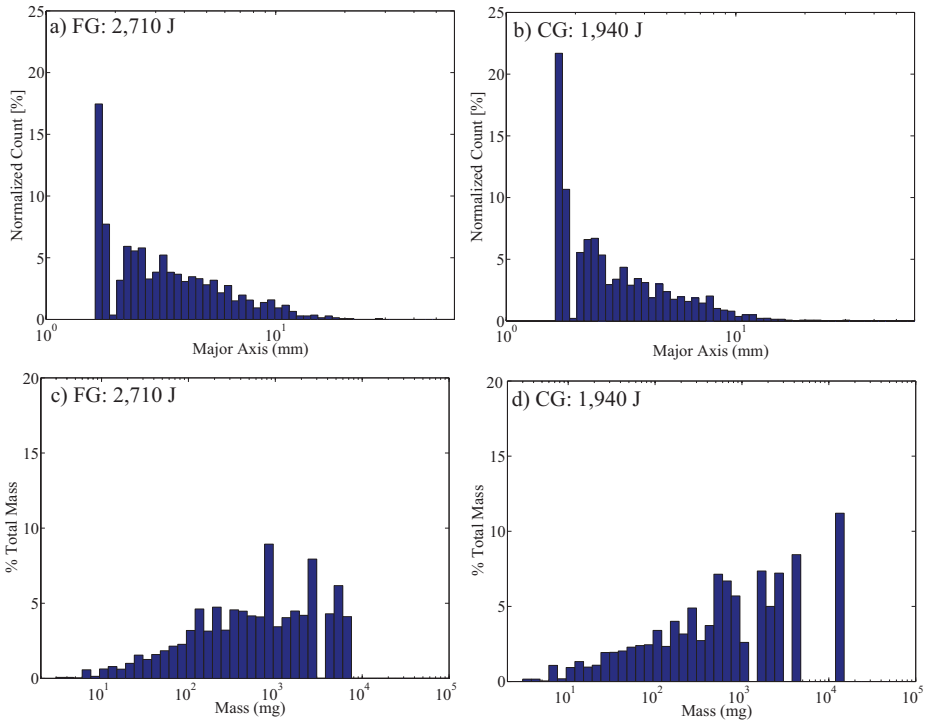

Fig. 7 Distribution of major axis dimensions for (a) FG: 2.7 kJ and (b) CG: 1.9 kJ, and the corresponding distributions of mass among mass groups.

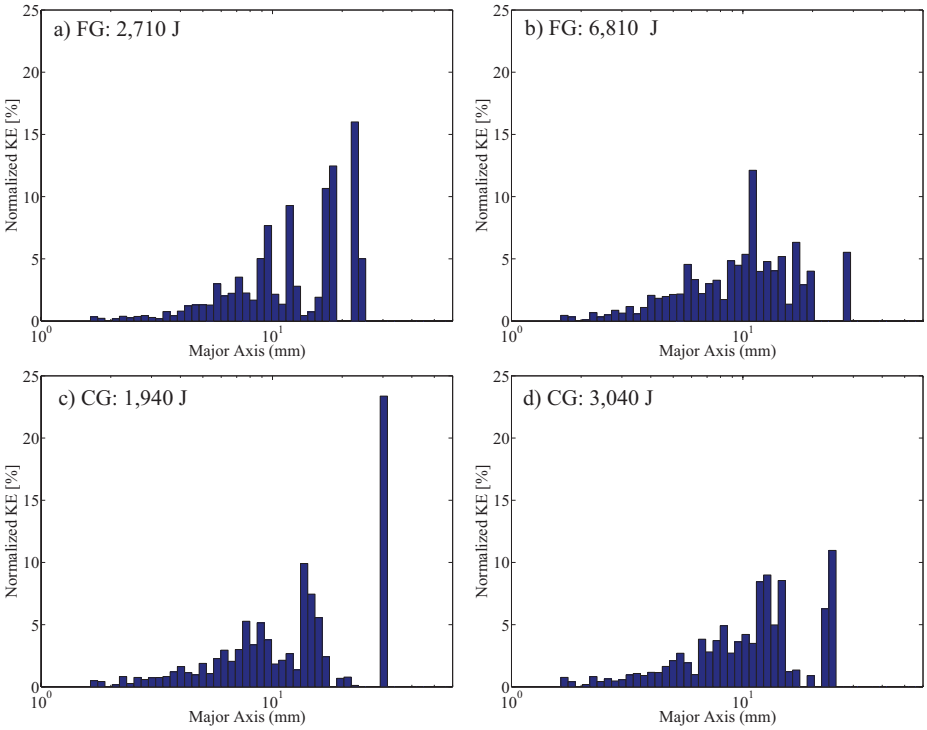

Fig. 8 Distribution of kinetic energy among major axis dimensions for (a) FG: 2.7 kJ, (b) FG: 6.8 kJ, (c) CG: 1.9 kJ and (d) CG: 3.0 kJ.

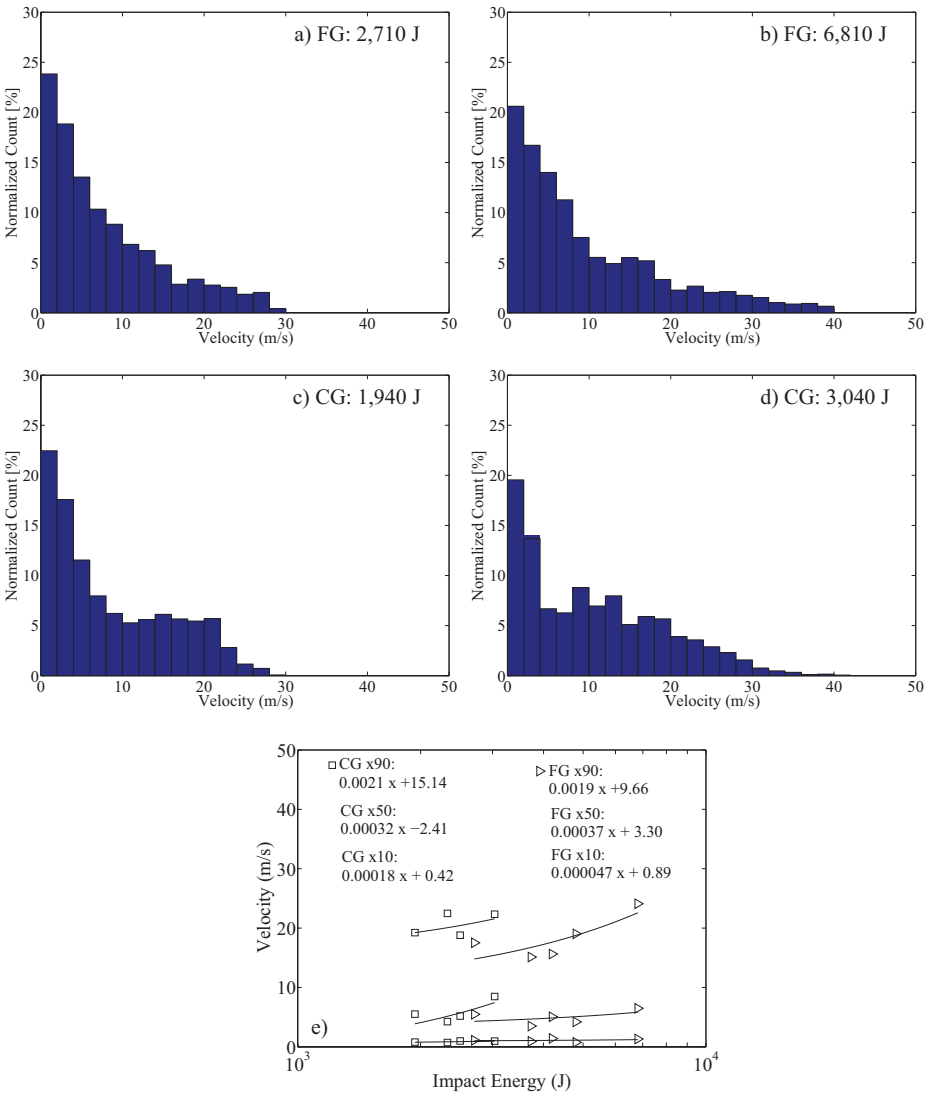

Fig. 9 Normalized distributions of ejecta number among velocity groups for: (a) FG: 2.7 kJ, (b) FG: 6.8 kJ, (c) CG: 1.9 kJ and (d) CG: 3.0 kJ. Percentile values of x_{10}, x_{50}, and x_{90} and curve fits for all impact energies are shown in (e).

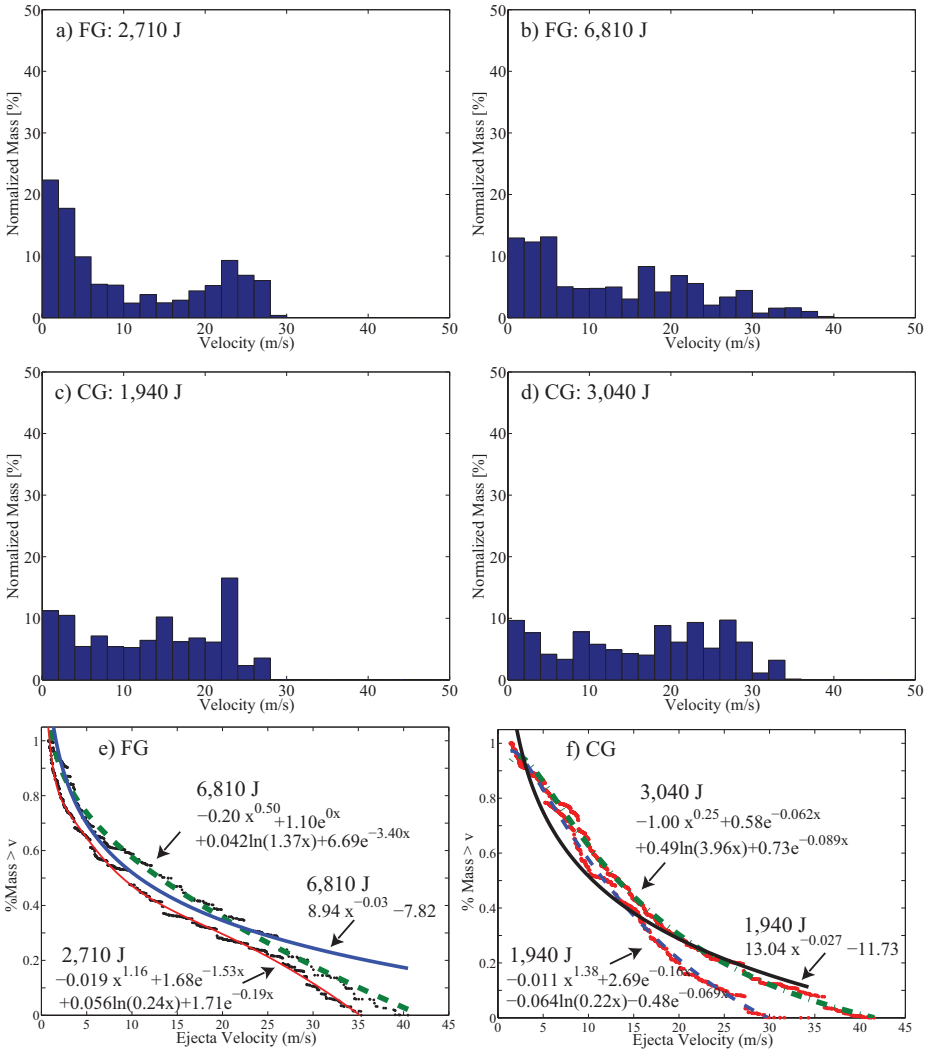

Fig. 10 Normalized distributions of mass among ejecta velocity groups for: (a) FG: 2.7 kJ, (b) FG: 6.8 kJ, (c) CG: 1.9 kJ and (d) CG: 3.0 kJ. The cumulative distribution of mass for ejecta velocity for the lowest and highest cases for (e) FG and (f) CG, as well as curve-fits. Black dots in (e) are the highest and lowest energy cases for FG, and red dots in (f) are the highes and lowest energy cases for CG. Fitted curves are various line types and colours.

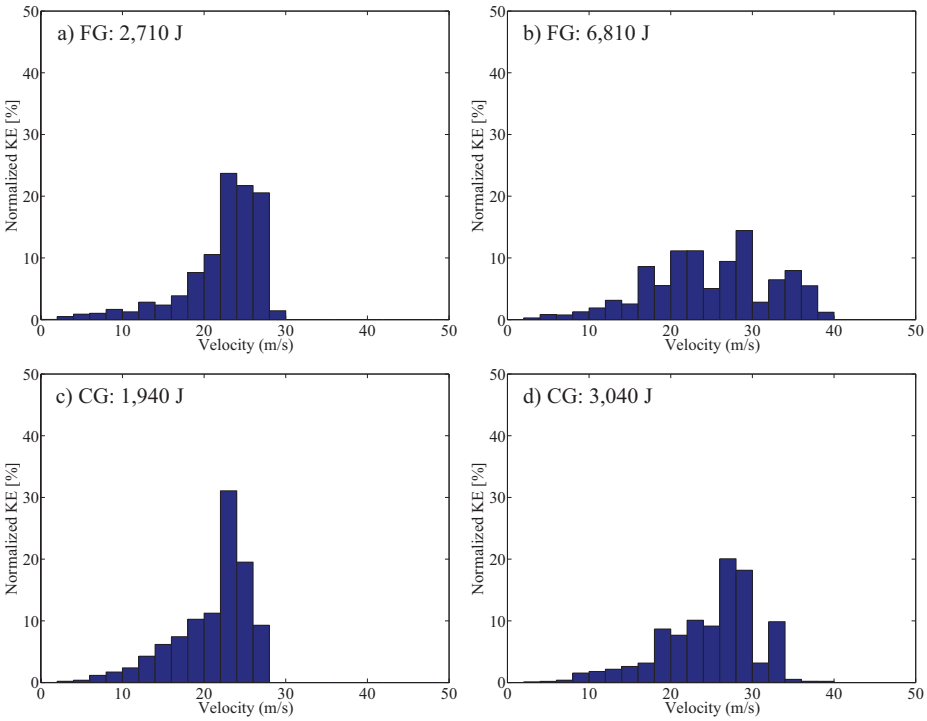

Fig. 11 Normalized distributions of kinetic energy among ejecta velocity groups for: (a) FG: 2.7 kJ, (b) FG: 6.8 kJ, (c) CG: 1.9 kJ and (d) CG: 3.0 kJ.

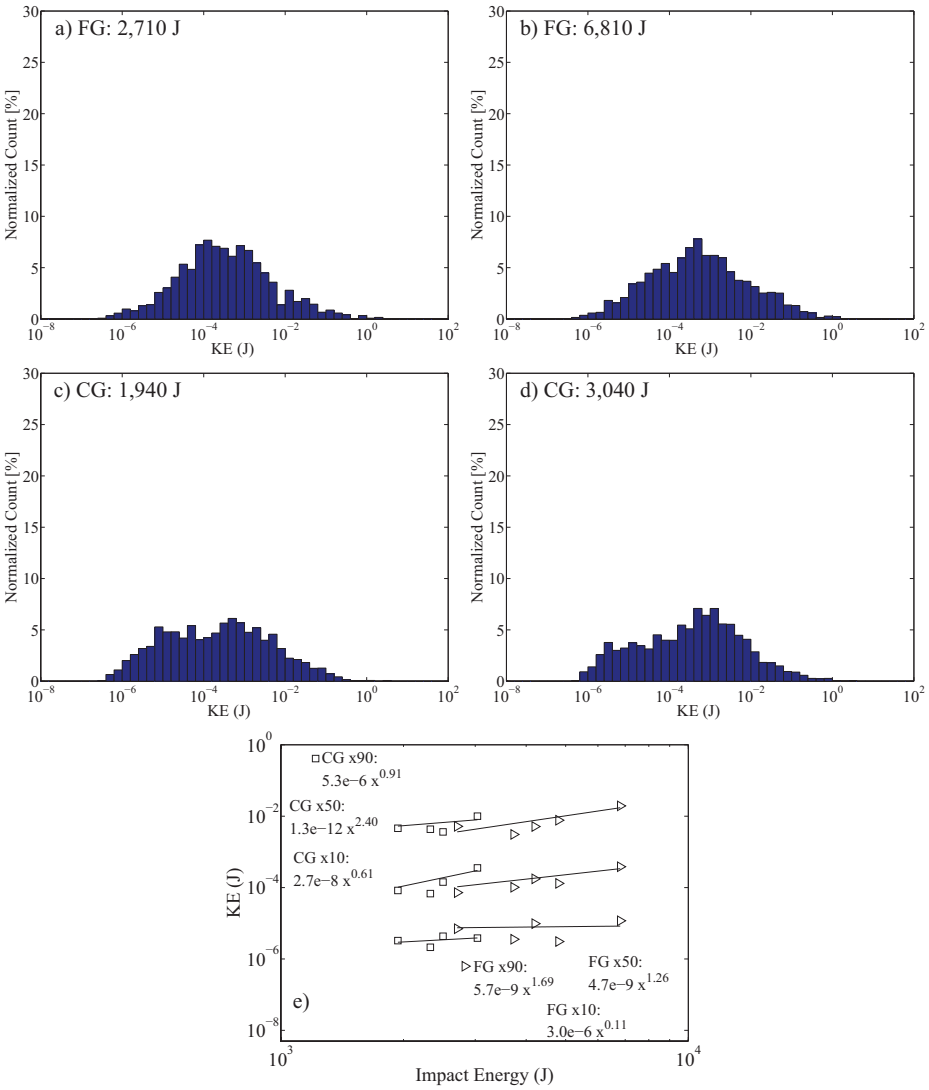

Fig. 12 Normalized distributions of ejecta kinetic energy for: (a) FG: 2.7 kJ and (b) FG: 6.8 kJ, and (c) CG: 1.9 kJ and (d) CG: 3.0 kJ. Values of x_{10}, x_{50}, and x_{90} with power-law fits are shown in (e).

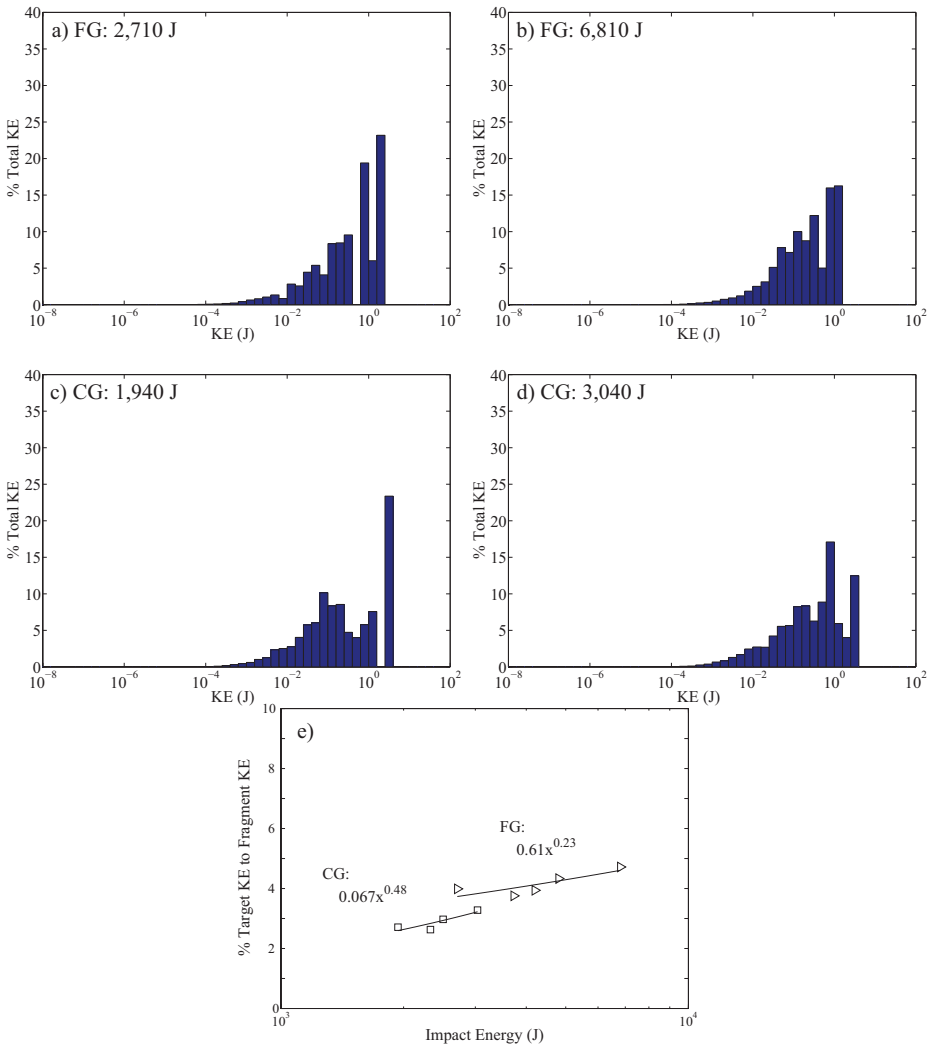

Fig. 13 Normalized distributions of kinetic energy among kinetic energy groups for: (a) FG: 2.7 kJ and (b) FG: 6.8 kJ, and (c) CG: 1.9 kJ and (d) CG: 3.0 kJ. The total percentage of impact energy transferred to ejecta kinetic energy is shown in (e).

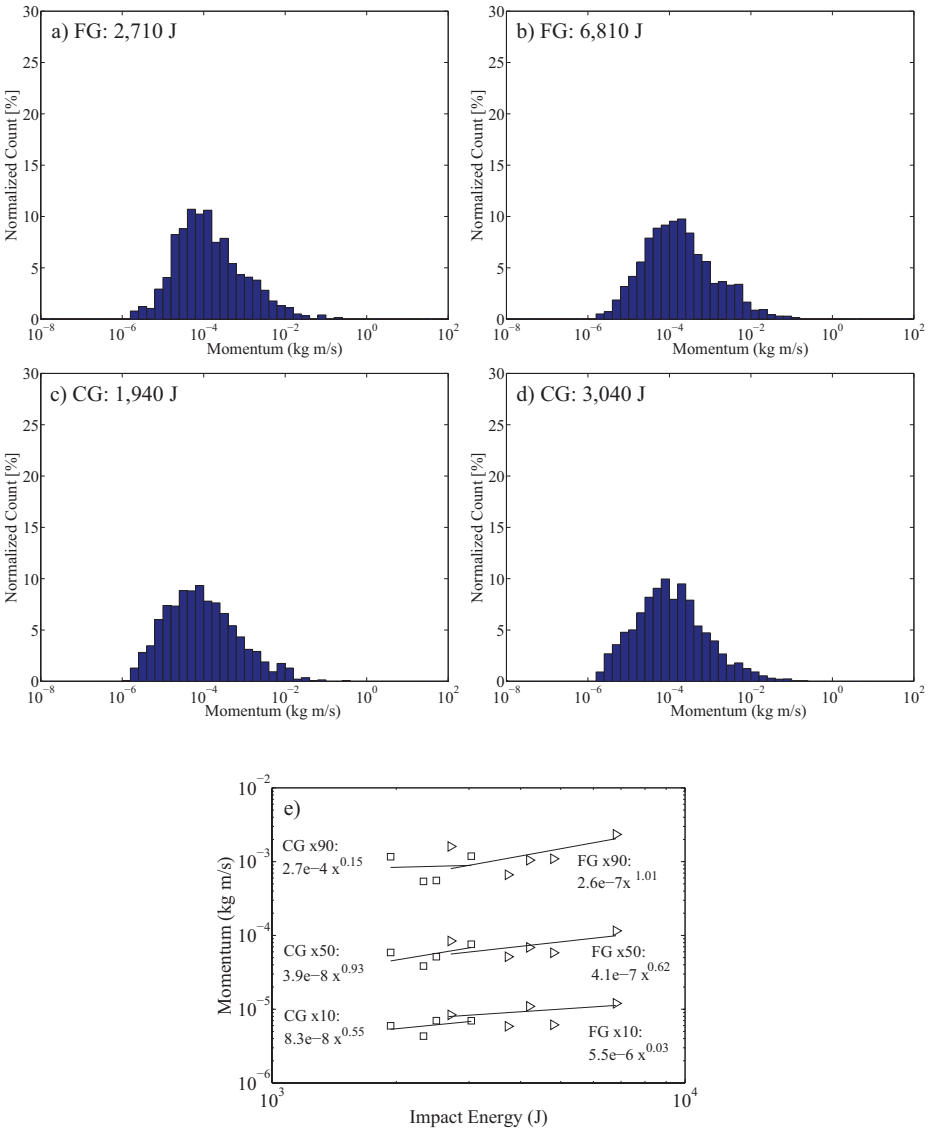

Fig. 14 Normalized distributions of momentum for: (a) FG: 2.7 kJ, (b) FG: 6.8 kJ, (c) CG: 1.9 kJ and (d) CG: 3.0 kJ. 10^{th}, 50^{th} and 90^{th} percentile are shown in (e) with power-law fits.

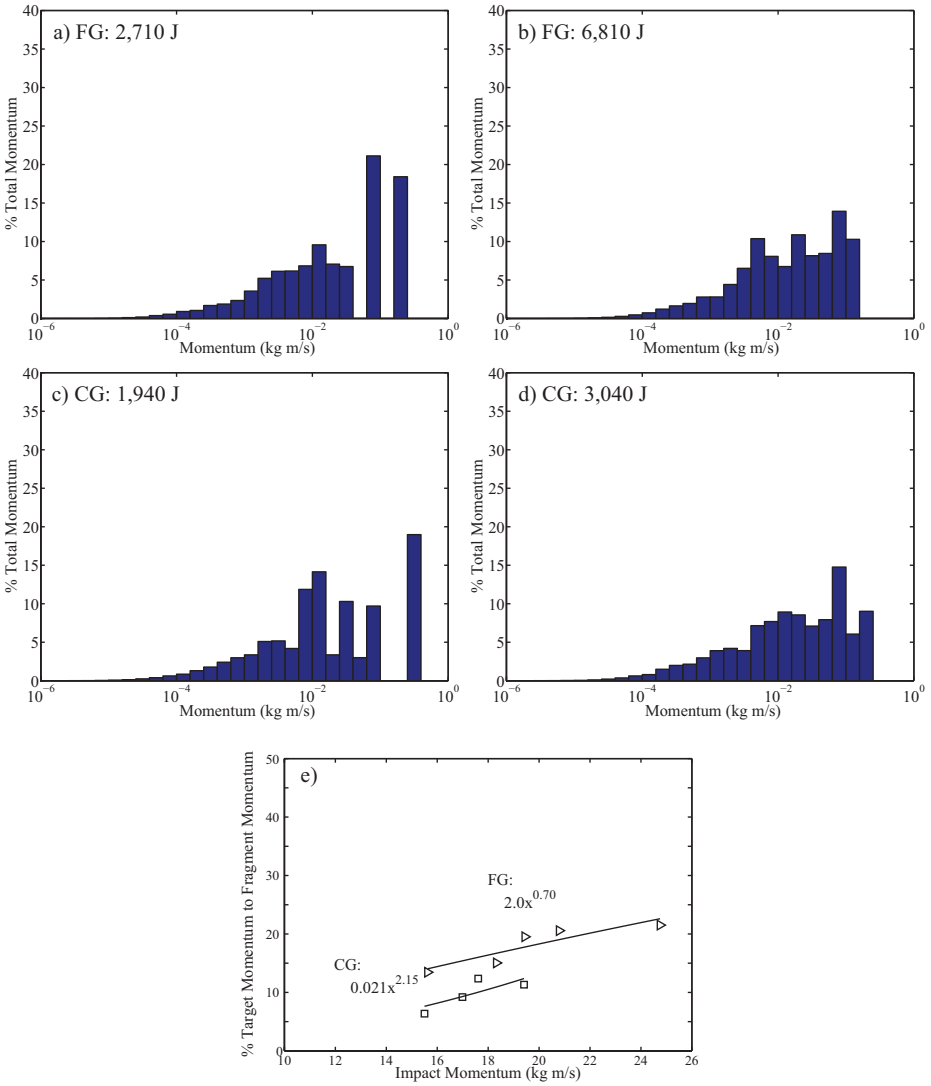

Fig. 15 Normalized distributions of momentum among momentum groups for: (a) FG: 2.7 kJ, (b) FG: 6.8 kJ, (c) CG: 1.9 kJ and (d) CG: 3.0 kJ. The total percentage conversion of incoming impactor momentum to ejecta momentum is shown in (e).

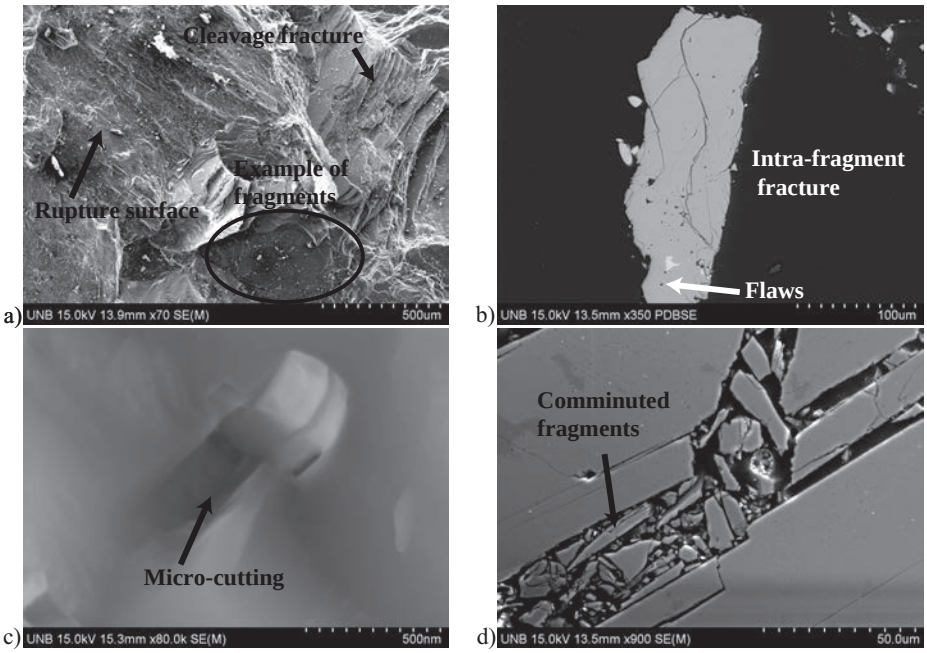

Fig. 16 SEM images: (a) complex fracture surface in plagioclase, (b) intra-fragment damage in plagioclase, (c) micro-cutting in quartz and (d) comminution in plagioclase.